Spectrochimica Acta Part A 94 (2012) 365–371

Spectrochimica Acta Part A: Molecular and Biomolecular Spectroscopy

journal homepage: www.elsevier.com/locate/saa

Structural, EPR, optical and Raman studies of Nd_2O_3:Cu^{2+} nanophosphors

B. Umesh[a,b], B. Eraiah[b,*], H. Nagabhushana[c,**], S.C. Sharma[c], B.M. Nagabhushana[d], C. Shivakumara[e], J.L. Rao[f], R.P.S. Chakradhar[g]

[a] Department of Humanities, PVP Polytechnic, Dr. AIT Campus, Bangalore 560 056, India
[b] Department of Physics, Bangalore University, Bangalore 560 056, India
[c] Prof C.N. R. Rao Centre for Nano Research, Tumkur University, Tumkur 572 103, India
[d] Department of Chemistry, M.S. Ramaiah Institute of Technology, Bangalore 560 054, India
[e] Solid State and Structural Chemistry Unit, Indian Institute of Science, Bangalore 560 012, India
[f] Department of Physics, Sri Venkateswara University, Tirupati 517 502, India
[g] National Aerospace Laboratories (CSIR), Bangalore 560 017, India

ARTICLE INFO

Article history:
Received 17 December 2011
Received in revised form 7 March 2012
Accepted 22 March 2012

Keywords:
Nanoparticles
PXRD
SEM
TEM
EPR
Raman
Optical properties

ABSTRACT

Nanocrystalline Nd_2O_3:Cu^{2+} (2 mol %) phosphors have been prepared by a low temperature solution combustion technique. Powder X-ray diffraction (PXRD) results confirm that hexagonal A-type Nd_2O_3 (900 °C, 3 h) and the lattice parameters have been evaluated by Rietveld refinement. Surface morphology of as-formed and Cu^{2+} doped Nd_2O_3 phosphors show that the particles are irregular in shape and porous in nature. TEM results also confirm the nature and size of the particles. The EPR spectrum exhibits two resonance signals with effective g values at $g_{||} \approx 2.12$ and $g_{\perp} \approx 2.04$. The g values indicate that the site symmetry of Cu^{2+} ions is octahedral symmetry with elongated tetragonal distortion. Raman studies show major peaks, which are assigned, to F_g and combination of $A_g + E_g$ modes. It is observed that the Raman peaks and intensity have been reduced in Cu^{2+} doped samples. UV–Visible absorption spectra exhibit a strong and broad absorption band at ~240 nm. Further, the absorption peak shifts to ~14 nm in Cu^{2+} doped samples. The optical band gap is estimated to be 5.28 eV for Cu doped Nd_2O_3 nanoparticles which are higher than the bulk Nd_2O_3 (4.7 eV). This can be attributed to the quantum confinement effect of the nanoparticles.

1. Introduction

In recent years Rare earths (RE) sesquioxides find wide applications in display devices, solid state lasers, X-ray radiography, luminescent materials. These materials show stable host for powerful lasers, high chemical, thermal stability and maximum power output. In particular Nd_2O_3 has been widely used in photonic applications [1–3], luminescent and thermoluminescent materials [4,5], protective coatings [6,7] and thin films [8]. In comparison with bulk neodymium oxide, Nd_2O_3 nanoparticles are of particular interest for many other potential applications due to their nanoscale dimension and large surface area.

Usually phosphor materials are prepared via solid state method by mixing of desired ingredients and followed by high temperature sintering (>1400 °C). In this method many problems occur such as poor sintering, non-homogeneity and difficult to control cation stoichiometry etc. Therefore, simple synthesis method is required to overcome these problems. In literature, different methods such as co-precipitation, sol-gel, hydrothermal are reported for the preparation of oxide materials [9,10]. However, these chemical methods involve complicated steps, such as precise control of pH and precipitation, in order to obtain the correct stoichiometric compound. On the other hand, combustion technique emerged in the last decade as an important synthesis technique for oxide nanoparticles for being very simple experimental set-up, fast, cost effective, ultra pure, large surface area and nano dimensional in size. There has been only one report on the synthesis of pure and Ce doped Nd2O3 using glycine as fuel [11]. In this paper we report first time Nd_2O_3:Cu^{2+} (2 mol%) nanopowders by a low temperature solution combustion technique with oxalyl di-hydrazide as fuel. The nanopowders are well characterized by powder X-ray diffraction (PXRD), scanning electron microscopy (SEM), Transmission electron microscopy (TEM) and Raman spectroscopy. Further, electron paramagnetic resonance (EPR), UV–Vis and photoluminescence (PL) have also been studied and the results are discussed in detail.

* Corresponding author. Mobile: +91 9449804014.
** Corresponding author.
E-mail addresses: eraiah@rediffmail.com (B. Eraiah), bhushanvlc@gmail.com (H. Nagabhushana).

1386-1425/$ – see front matter © 2012 Elsevier B.V. All rights reserved.
http://dx.doi.org/10.1016/j.saa.2012.03.057

2. Experimental

2.1. Synthesis of Nd_2O_3:Cu^{2+} (2 mol%) phosphors

An aqueous solution containing stoichiometric amounts of analar grade neodymium nitrate ($Nd(NO_3)_3$), copper nitrate ($Cu(NO_3)_2$) and oxalyl dihydrazide ($C_2H_6N_4O_2$; ODH) fuel was dissolved in a minimum quantity of doubled distilled water in a cylindrical Petri dish of approximate 150 ml capacity. ODH used in the combustion synthesis was prepared in our laboratory by the reaction of diethyl oxalate and hydrazine hydrate as described in the literature [12]. The mixture was dispersed well using a magnetic stirrer for about 5 min. Then, the Petri dish with heterogeneous mixture was placed into a pre-heated muffle furnace maintained at 400±10 °C. Initially, the reaction mixture underwent thermal dehydration and ignition with liberation of large gaseous products such as oxides of nitrogen and carbon. Finally, voluminous and foamy light greenish product was obtained. Theoretical equation assuming complete combustion of the redox mixture used for the synthesis of Nd_2O_3 may be written as

$$2Nd(NO_3)_3 + C_2H_6N_4O_2 \rightarrow Nd_2O_3 + 2CO_2 + 5N_2 + 3H_2O \quad (1)$$

2.2. Instruments

The phase purity of the nanophosphors is examined by powder X-ray diffractometer (PXRD) (PANalytical X'Pert Pro) using Cu K_α radiation with a nickel filter. The surface morphology of the phosphor has been examined using scanning electron microscope (JOEL JSM 840 A) by sputtering technique with gold as covering contrast material. Transmission electron microscope (TEM) analysis was performed on a Hitachi H-8100 (accelerating voltage upto 200 kV, LaB_6 Filament) equipped with EDS (Keney Sigma TM Quasar, USA). UV–VIS absorption of the samples was recorded on SL 159 ELICO UV–VIS Spectrophotometer. The photoluminescence (PL) measurements were performed on a Shimadzu Spectroflourimeter (Model RF 510) equipped with 150 W Xenon lamp as an excitation source. Raman spectroscopic studies were performed on Renishaw In-Via Raman spectrometer with 633 nm He–Cd laser and a Leica DMLM optical microscope equipped with 50× objective, thus providing a laser spot of 2 μm in diameter. The FT-IR studies have been performed on a Perkin Elmer Spectrometer (Spectrum 1000) with KBr pellets. The EPR spectra were recorded at room temperature on a JEOL-FE-1X EPR spectrometer operating in the X-band (about 9.2 GHz) with a filed modulation frequency of 100 kHz. The magnetic field was scanned from 0 to 500 mT and the microwave power used was 5 mW. A powdered phosphor of 100 mg was taken in a quartz tube for EPR measurements.

3. Results and discussion

3.1. Powder X-ray diffraction

Fig. 1 shows the powder X-ray diffraction pattern of (a) as-formed Nd_2O_3, (b) Nd_2O_3 calcined at 900 °C, (c) as formed Nd_2O_3:Cu and (d) Nd_2O_3:Cu calcined at 900 °C respectively. The XRD patterns show amorphous Nd_2O_3 phase along with neodymium oxide carbonate (Nd_2CO_3) peaks (JCPDS No-37-0806). After heat treated at 900 °C for 3 h, the PXRD pattern of combustion derived product has been changed to hexagonal phase with A-type of Nd_2O_3 (Fig. 1b). The hexagonal phase diffraction peaks are readily indexed with JCPDS file No 83-1353. The formulation of Nd_2CO_3 phase might be due to the reaction between Nd_2O_3 and CO_2 products at the calcinated temperature during combustion reaction.

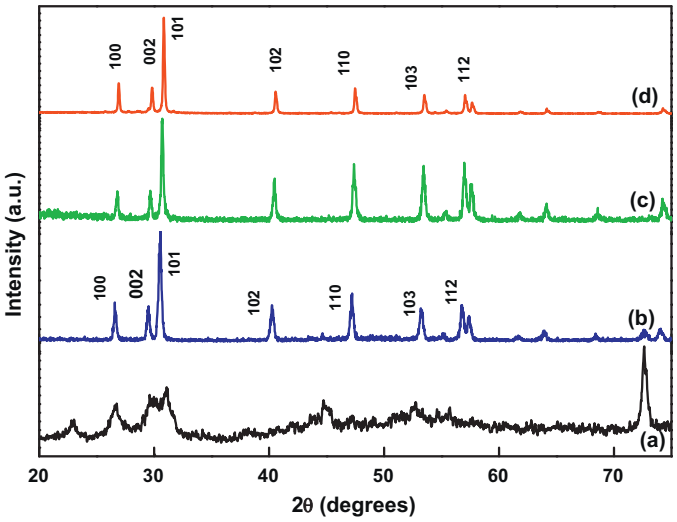

Fig. 1. XRD patterns for (a) as-formed Nd_2O_3, (b) Nd_2O_3 calcined at 900 °C, (c) as formed Nd_2O_3:Cu and (d) Nd_2O_3:Cu calcined at 900 °C.

$$Nd_2O_3 + CO_2 \rightarrow Nd_2O_3(CO_3)_2 \quad (2)$$

When the sample is calcined at 900 °C for 3 h, the intensity of the diffraction peaks increase which suggests that the sample is now well crystallized. The average crystallite size of the products were estimated using Scherer's formula and found to be in the range 19–30 nm for calcined sample, whereas for Cu^{2+} doped sample the average crystallite size was found in the range 15–45 nm.

The strain and crystallite size produces peak broadening in the diffraction pattern. The crystallite and strain effect have to be differentiated in the diffraction pattern. Both effects are independent and can be distinguished by W–H plots. As prepared PXRD pattern shows asymmetry, this may be due to the lattice strain [13]. However, for the sample calcined at 900 °C, the lattice strain is reduced. Since the heat treated sample is well crystalline and single phase (hexagonal phase), the crystallite size and the strain can be estimated from W–H method [14]. The W–H equation is given by

$$\beta_{hkl} \cos\theta_{hkl} = \frac{k\lambda}{d} + 2\varepsilon \sin\theta_{hkl} \quad (3)$$

where k is the shape factor which is 0.9 for uniform small size crystals, λ the wave length of X-ray, θ_{hkl} is the Bragg's angle, ε is the strain, β_{hkl} is the full width at half maxima of the corresponding hkl planes and d is the average crystallite size measured in the direction perpendicular to the surface of the specimen. The graph is plotted between sin θ_{hkl} and β_{hkl} cos θ_{hkl} for un-doped and Cu doped Nd_2O_3 and is shown in Fig. 2. The value of the strain is calculated from the slope of the line which is 1.15×10^{-3} for un-doped calcined sample, however, in Cu^{2+} doped heat treated sample strain was found to be 1.30×10^{-3}. The estimated crystallite size is in well agreement with those obtained from Scherer's formula. The strain values obtained from the W–H plots are very small and hence have negligible effect on XRD broadening.

The Rietveld refinement is a method in which the profile intensities obtained from step-scanning measurements of the powders allow to estimating an approximate structural model for the real structure. This was performed with a FULLPROF program [15,16]. We have utilized the pseudo-voigt function in order to fit the several parameters to the data point: one scale factor, one zero shifting, four back ground, three cell parameters, five shape and width of the peaks, one global thermal factor and two asymmetric factors. A typical analysis of the sample is shown in Fig. 3 which

Table 1
Rietveld refinement results and atomic co-ordination employed to model the Nd_2O_3 unit cell.

Atoms	Wyckoff notations	X	Y	Z	Occupancy
Nd^{3+}	2d	0.3333	0.6666	0.2494(8)	0.98
Cu^{2+}	2d	0.3333	0.6666	0.2494(8)	0.02
O_2^{-2}	1a	0.0000	0.0000	0.0000	1
O_1^{-2}	2d	0.3333	0.6666	0.6495(2)	1

Crystal System: Hexagonal, Space group: *P63/mmc* (No. 194).
$a = 3.8306(2)$ Å, $c = 6.0006(4)$ Å, $V = 76.25(8)$ (Å)^3, $R_p = 10.5$, $R_{wp} = 15.4$, $\chi^2 = 1.59$, $R_{Bragg} = 5.40$, $R_F = 3.56$.

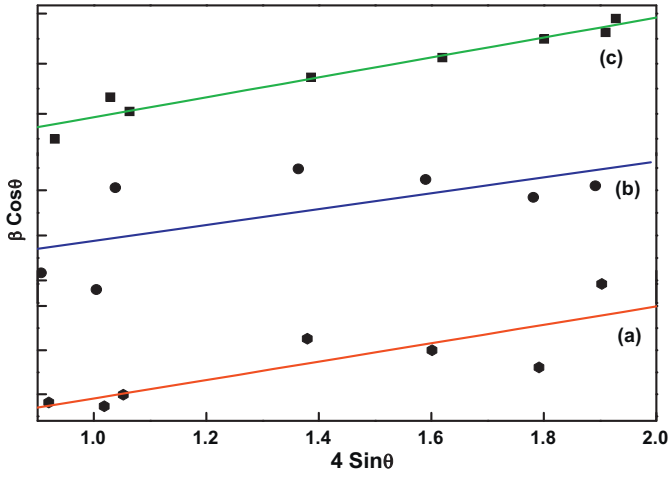

Fig. 2. W–H plots of (a) Nd_2O_3 calcined at 900 °C, (b) Nd_2O_3:Cu (as-formed) and (c) Nd_2O_3:Cu calcined at 900 °C.

presents the experimental and calculated PXRD patterns obtained by the refinement of hexagonal A-type Nd_2O_3. The corresponding packing diagram of Nd_2O_3:Cu^{2+} (2 mol%) is shown in Fig. S1. The refined parameters such as occupancy, atomic functional positions are summarized in Table 1. In this table, the fitting parameters

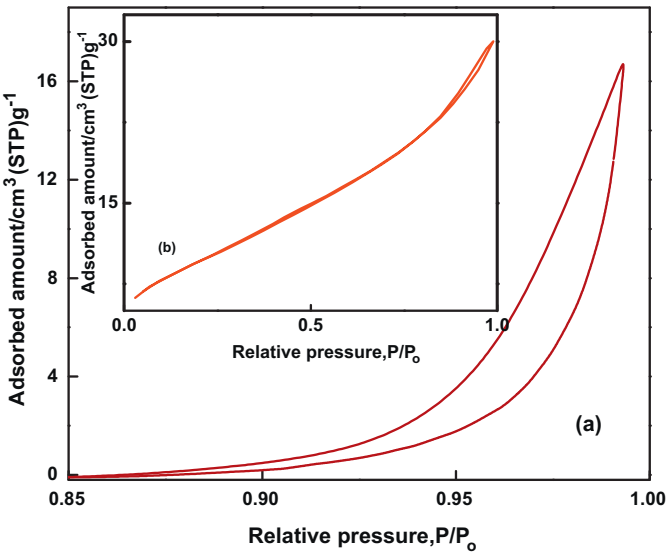

Fig. 4. BET Surface area of (a) Nd_2O_3:Cu (as-formed), (b) Nd_2O_3:Cu calcined at 900 °C.

(R_p, R_{wp} and χ^2) indicate a good agreement between the refined and observed XRD patterns for the C-type Nd_2O_3. The refined lattice parameter values $a = 3.8306(2)$ Å $c = 6.0006(4)$ Å, cell volume 76.25(8) (Å)^3 confirmed that the Nd_2O_3 has a hexagonal structure. These values are in well agreement with those obtained in the literature [17].

3.2. Surface area measurement

The N_2 adsorption–desorption measurement at a liquid N_2 temperature was used to study the porosity of the undoped Nd_2O_3. Fig. 4 depicts the N_2 adsorption–desorption isotherms of un-doped (inset) and Cu doped Nd_2O_3 nanophosphor. The isotherm exhibits a type II sorption behavior without the existence of hysterias loop indicating the presence of macro porous structural characteristic

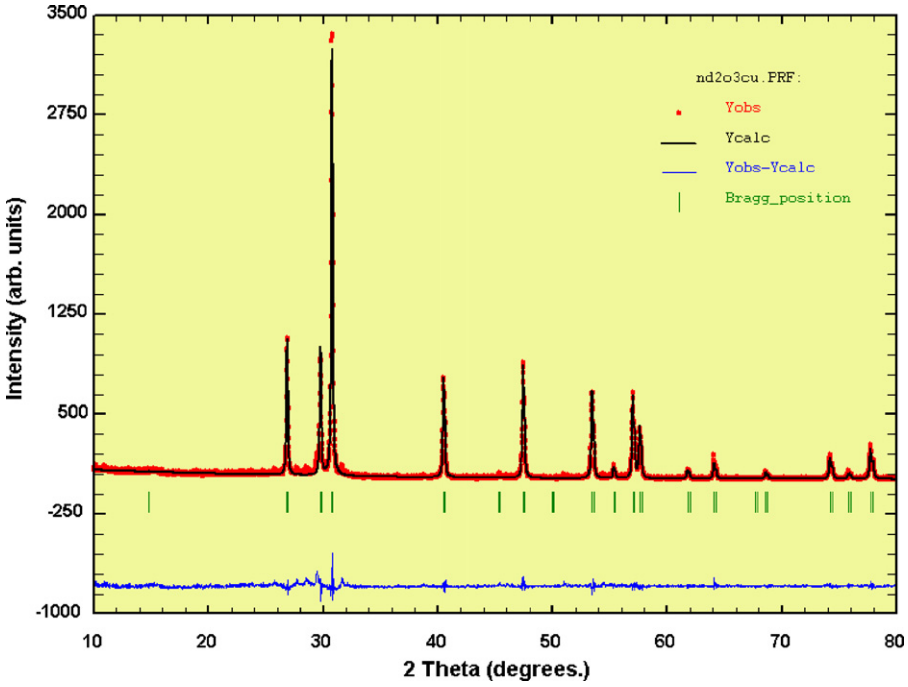

Fig. 3. Rietveld refinement of Cu doped Nd_2O_3 calcined at 900 °C.

according to the classification of IUPAC [18]. However, in Cu doped samples, the isotherm shows a type IV like sorption behavior with predominant mesoporous structure [3] with apparent hysteris loop as shown in the figure. The apparent step in the adsorption branch combined with the sharp decline in the desorption branch is an obvious verification of the presence of mesoporosity [19]. An abrupt increase in adsorption volume of adsorbed N_2 was observed and located in P/P_0 value greater than 0.5. This sharp increase is typically ascribed to the result of capillary condensation, indicating the good homogeneity of the sample and fairly small pore size since the P/P_0 position of the inflection point is related to the pore size. The isotherms are well matched to Nd_2O_3 synthesized by sol–gel method [20].

The formation of a hexagonal phase Nd_2O_3 nanoparticles was further supported by Raman spectroscopy [21]. According to the Raman line broadening the particle size of the Nd_2O_3 can be estimated using the relation

$$\Gamma\ (\mathrm{cm}^{-1}) = 10 + \frac{124.7}{d_g} \quad (4)$$

where $\Gamma(\mathrm{cm}^{-1})$ is the full width at half maximum of the Raman peaks and d_g is the particle size. The particle size (d_g) of the heat treated and Cu doped Nd_2O_3 nanoparticles is observed to be 18 & 45 nm respectively, which are in good agreement with the particle size observation with the transmission electron microscopy image and calculated from PXRD using Scherer's method.

3.3. Scanning and transmission electron microscopy (SEM & TEM)

The surface morphology of as-formed, Cu (2 mol%) doped Nd_2O_3 and heat-treated at 900 °C, 3 h powders were shown in Fig. S2. The SEM micrograph of the as formed product shows that the particles are agglomerated, crispy and porous. This porous in nature is typical for combustion synthesized powders due to rapid release of gaseous byproducts during combustion synthesis [22]. However, in Cu doped samples, the particles are observed to be spherical in shape with less agglomeration. The same was confirmed from TEM results. A TEM image of Cu doped Nd_2O_3 phosphor synthesized by combustion method is shown in Fig. S3. The particles are spherical in shape, which varies from 30 to 80 nm. These spherical shaped particles are easy to be packed densely so that screen and displays can obtain high definition and these dense packed small particles can prevent the phosphor from ageing.

3.4. UV–Visible spectroscopy and band gap (E_g) measurements

Fig. 5 shows the UV–Visible spectra of (a) as-formed Nd_2O_3 (b) heat-treated Nd_2O_3 at 900 °C (c) Nd_2O_3:Cu (as formed) (d) Nd_2O_3:Cu (heat treated at 900 °C). The absorbance is expected to depend on several factors such as band gap, oxygen deficiency surface roughness and impurity centers. Absorbance spectra shows an UV cutoff around 250–290 nm which can be attributed to the photo excitation of electrons from valence band to conduction band [23]. The absorption edge of different samples varies as the concentration of Cu in the Nd_2O_3 nano particles varies.

The optical band gap energy (E_g) (Fig. 6) was estimated by the method proposed by Wood and Tauc [24]. According to these authors, the optical band gap is estimated with absorbance and photon energy by the following equation

$$\alpha h\nu\, \alpha (h\nu - E_g)^k \quad (5)$$

where α is the absorbance, h is the Plancks constant, ν is the frequency, E_g is the optical band gap and k is the constant associated to the different types of electronic transitions $k = ½, 2, 3/2, 3$ for direct allowed, indirect allowed, direct forbidden and indirect forbidden transitions respectively. According to literature [25] the

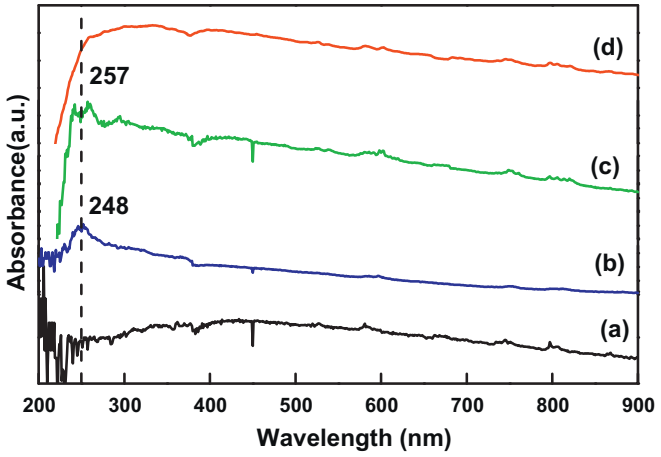

Fig. 5. UV–Vis spectra of (a) as-formed Nd_2O_3, (b) heat-treated Nd_2O_3 at 900 °C, (c) Nd_2O_3:Cu (as formed) and (d) Nd_2O_3:Cu (heat treated at 900 °C).

oxides are characterized by an indirect allowed electronic transition and hence, the $k = 2$ value was adopted as standard in equation (5). Thus, the E_g values were evaluated by extrapolating the linear portion of the curve or tail [$(h\nu\alpha)^{1/k} = 0$] in the UV–Vis absorbance spectra.

A plausible explanation for the variations observed in the E_g values can be related to the degree of structural order–disorder into the lattice, which is able to change the intermediary energy level distribution within the band gap. The variations in the band gap values might also be due to higher degree of structural defects, while the phosphor heat treated at 900 °C (Fig. 6d), the absorption spectrum show more ordered. On the basis of this information, the structure becomes more ordered with the heat treated temperature i.e. when the concentration of structural defects (oxygen vacancies, distortions and/or strains in the lattice) is reduced. The presence of intermediary energy levels (deep and shallow holes) is minimized within the optical band gap and consequently, the E_g values increase. As it can be seen the energy band gap values (Table 2) are mainly dependent on the preparation methods and experimental

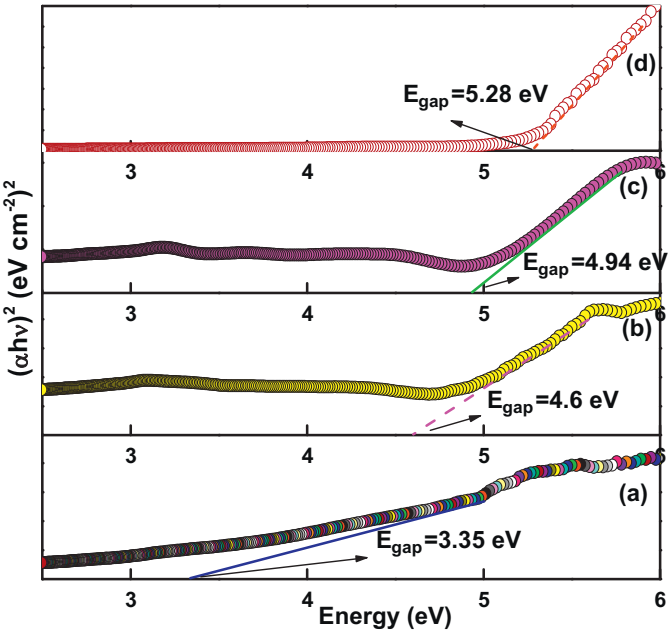

Fig. 6. Energy band-gap of (a) as-formed Nd_2O_3, (b) heat-treated Nd_2O_3 at 900 °C, (c) Nd_2O_3:Cu (as formed) and (d) Nd_2O_3:Cu (heat treated at 900 °C).

Table 2
Crystallite size, band gap and strain of un-doped and Cu (2 mol%) doped Nd_2O_3 nanopowders.

Sample	Grain size (nm)		Band gap (eV)	Strain ($\times 10^{-3}$)
	Scherer's method	W–H method		
Nd_2O_3 (as-formed)	–	–	3.35	–
Nd_2O_3 (calcined at 900 °C)	18	19	4.6	1.15
Nd_2O_3:Cu (2 mol%)	17	18	4.94	1.06
Nd_2O_3:Cu (calcined at 900 °C for 3 h)	45	49	5.28	1.30

conditions (heat-treated and processing time). In particular, these key factors can favour or inhibit the formation of structural defects, which are able to control the degree of structural order–disorder in the material and consequently, the number of intermediary energy levels within the band gap.

The measured band gap values was found to be 5.28 eV for Cu doped Nd_2O_3 nanoparticles which are higher than the required value of bulk Nd_2O_3 4.70 eV. This can be attributed to the quantum confinement effect of the nano particles. The absorption edge of Nd_2O_3 shifts towards higher wavelength after Cu doping. Furthermore such a red shift depends linearly on the content. This observation shows that the absorption edge of Nd_2O_3 can be engineered towards higher wavelength by introduction of Cu content. The UV–Vis spectra are recorded to resolve the correlation between the size and absorption edge of the Nd_2O_3 nanoparticles. The wide absorption peak occurred in wavelength range of 600–700 nm due to the oxygen vacancies in Nd_2O_3 samples. Absorption peaks present a distinct red shift of samples. This may be due to particle size increases at higher temperatures. The carriers of electrons and holes are confined in a very small region, and coupling interaction is enhanced with each other.

3.5. Photoluminescence (PL)

Fig. 7 shows the typical room temperature PL spectrum of Cu doped Nd_2O_3 nanophosphor. PL spectrum of Cu doped Nd_2O_3 sample consists of two luminescent peaks, one in the UV band centered at 380 nm and another weak green bands in the range 503–523 nm. The UV emission also known as near band edge emission (NBE) originates due to recombination of free exciton through an exciton–exciton collision process while visible emission known as deep level emission (DPE) attributed to the single ionized oxygen vacancy and arises from recombination of a photo generated hole with single ionized charged state of the defect in oxide phosphors [26]. Similar PL emission peaks observed in hexagonal Cu doped ZnO nanophosphor [23]. Several researchers suggested that Cu impurity is responsible for green emission in oxide phosphors [27]. Cu may exist in Cu^+ and Cu^{2+} state if the dopant is in monovalent state then it will give structureless emission which is due to donor–acceptor pair recombination involving the copper acceptor and a shallow donor impurity. But in presence of divalent copper ion green emission peak is generated due to a short lived transfer of an electron from neighboring oxygen to the copper ion [28].

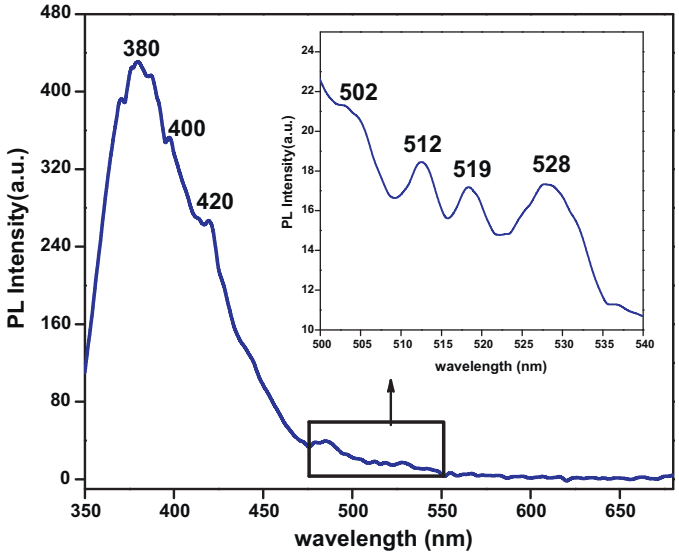

Fig. 7. PL spectra of (a) Nd_2O_3:Cu (calcined at 900 °C) and (b) magnified PL spectrum in the range 475–540 nm (inset).

3.6. Electron paramagnetic resonance (EPR)

Fig. 8 shows the electron paramagnetic resonance (EPR) spectrum of Nd_2O_3:Cu (2 mol%) phosphor recorded at room temperature. The EPR spectra of Cu^{2+} ions in this phosphor could be analyzed by using an axial spin-Hamiltonian [29]. The EPR spectrum exhibits two resonance signals with effective g values at $g_{||} \approx 2.12$ and $g_{\perp} \approx 2.04$. The g values indicate that the site symmetry of Cu^{2+} ions is octahedral symmetry with elongated tetragonal distortion.

3.6.1. Population of spin levels (N)

The population of spin concentration (N) can be calculated by comparing the area under the absorption curve with that of a standard ($CuSO_4{\cdot}5H_2O$ in this study) of known concentration. Weil et al. [30] gave the following expression which includes the experimental parameters of both sample and standard.

$$N = \frac{A_x(Scan_x)^2 G_{std}(B_m)_{std}(g_{std})^2[S(S+1)]_{std}(P_{std})^{1/2}}{A_{std}(Scan_{std})^2 G_x(B_m)_x(g_x)^2[S(S+1)]_x(P_x)^{1/2}}[std] \quad (6)$$

where A is the area under the absorption curve, which can be obtained by double integrating the first derivative EPR absorption curve, Scan is the magnetic field corresponding to a unit length of the chart, G is the gain, B_m is the modulation field width, g is the g factor, S is the spin of the system in its ground state. P is the power of the microwave source. The subscripts 'x' and 'std' represent the corresponding quantities for the Nd_2O_3:Cu^{2+} powder and the

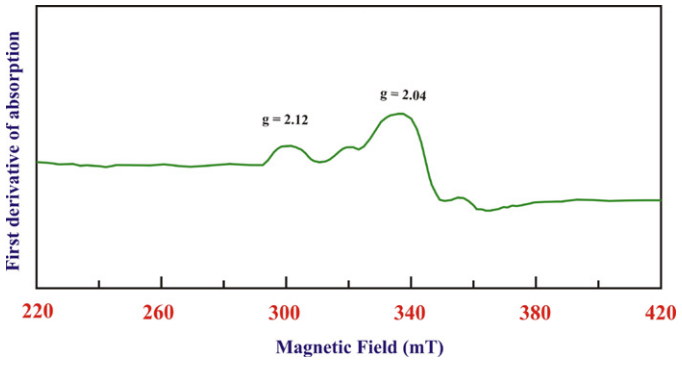

Fig. 8. EPR Spectrum of Nd_2O_3:Cu (2 mol%) (calcined at 900 °C) at room temperature.

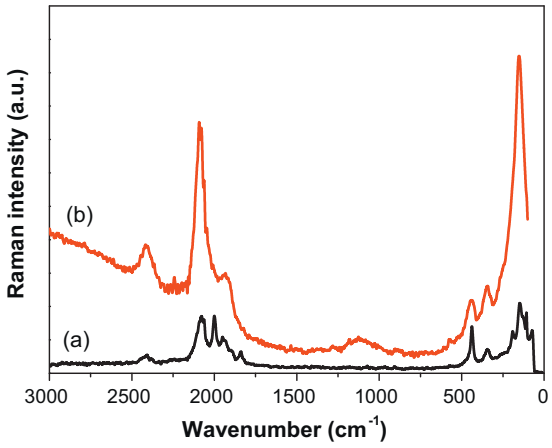

Fig. 9. Raman spectrum of (a) as formed Nd_2O_3 and (b) Nd_2O_3:Cu^{2+} (calcined at 900 °C for 3 h).

reference ($CuSO_4{\cdot}5H_2O$) respectively. By using the above expression the number of spins participating in resonance (N) has been evaluated and is found to be 3.12×10^{16} spins/m^3.

3.6.2. Calculation of paramagnetic susceptibility (χ) from EPR data

The magnetic susceptibility (χ) of Cu^{2+} ions in Nd_2O_3 has been calculated at room temperatures using the expression [31].

$$\chi = \frac{Ng^2\beta^2 J(J+1)}{3K_B T} \tag{7}$$

where N is the number of spins per m^3, g is spectroscopic splitting factor, β is the Bohr magneton, K_B is the Boltzmann constant and $J = 5/2$. The number of spins 'N' can be calculated by double integrating the first derivative EPR spectrum and $g = (g_{||} + 2g_{\perp})/3$ is taken from EPR data. The paramagnetic susceptibility (χ) was calculated at room temperatures and is found to be 7.9527×10^{-7} m^3/kg.

3.7. Raman spectroscopy

The Raman spectra of undoped and Cu (2 mol%) doped Nd_2O_3 nanophosphor is shown in Fig. 9. All the spectra for the as formed Nd_2O_3 are dominated by the presence of strong peaks located at 105, 150, 190, 344 and 440 cm^{-1} in the lower wavenumber region and the peaks at 1840, 1946, 1999, 2083, and 2407 cm^{-1} in the higher wavenumber region. According to factor group theory 22 active Raman modes have been predicted for the Nd_2O_3 A-type structure. The major peaks observed are assigned to F_g mode and combination of $A_g + E_g$ modes and similarly in 22 Raman modes have in C type bixbyite structured rare earth sesquioxides, out of which $4A_g$, $4E_g$ and $14F_g$ are Raman active modes [32,33]. From the figure it is observed that the Raman modes exhibit a blue shift of ~13 cm^{-1} in Cu^{2+} doped samples. The blue shift is believed to originate from the residual stress along the C-axis due to lattice distortion. Moreover, this vibration peaks becomes stronger and wider in Cu doped samples, indicating that more oxygen vacancies appear after Cu incorporation in to the Nd_2O_3.

Further, it is well known that in the case of nano systems, the Raman frequency undergoes a red shift with a decrease in the radius of nano solid. Pan et al. [23] suggested that this red shift arises from the cohesive bond weakening of the lower coordinated atoms near the surface region of the nanograin. Another factor responsible for this shift may be the short range interactions between a phonon and photon which describe the covalent bonding and thus are correlated to bond energy and bond length. Another factor governing this shift may be that when the size is decreased the momentum conservation will be relaxed and the Raman active modes will not be limited at the center of the Brillounin zone. Hence, from the above results it may be concluded that there is a decrease in Raman wavenumber in the case of rare earth sesquioxides when in comparison with bulk.

4. Conclusions

Nd_2O_3:Cu^{2+} (2 mol%) nanophosphors have been successfully prepared by a low temperature solution combustion method using ODH as fuel. PXRD of un-doped sample shows amorphous Nd_2O_3 phase along with neodymium oxide carbonate peaks. After heat treated at 900 °C for 3 h, the PXRD pattern has been changed to hexagonal phase with A-type of Nd_2O_3. The particle size of un-doped and Cu doped Nd_2O_3 heat treated samples have been calculated by Williamson–Hall (W–H) plots as well as Scherrer's method and are found to be in the range of 19–30 nm and 15–45 nm respectively. TEM image also confirms the nanocrystalline nature of Cu doped Nd_2O_3. SEM micrographs of un-doped and Cu doped Nd_2O_3 show highly porous, agglomeration with large voids. The optical band gap of Cu doped Nd_2O_3 nanoparticles is 5.28 eV which is higher than the bulk Nd_2O_3 4.7 eV. This can be attributed to the quantum confinement effect of the nano particles. The EPR spectrum shows two resonance signals with effective g values at $g_{||} \approx 2.12$ and $g_{\perp} \approx 2.04$. The g values indicate that the site symmetry of Cu^{2+} ions is octahedral symmetry with elongated tetragonal distortion. Raman study show major peaks, which are assigned, to F_g and combination of $A_g + E_g$ modes. PL spectrum of Cu doped Nd_2O_3 sample consists of two luminescent peaks one in the UV band centered at 380 nm and another weak green bands in the range 503–523 nm. The UV emission also known as near band edge emission (NBE) originates due to the recombination of the free exciton through an exciton–exciton collision process while visible emission known as deep level emission (DPE) attributed to the single ionized oxygen vacancy and arises from recombination of a photo generated hole with single ionized charged state of the defect in oxide phosphors.

Acknowledgments

The authors are grateful to TEQIP Lab of M. S. Ramaiah Institute of Technology, Bangalore for providing facilities for preparation of materials. One of the authors B.U. acknowledges Management P. V. P Polytechnic, Bangalore for the support and encouragement. Prof. J. L. Rao is thankful to University Grants Commission for the award of Emeritus Fellowship.

Appendix A. Supplementary data

Supplementary data associated with this article can be found, in the online version, at http://dx.doi.org/10.1016/j.saa.2012.03.057.

References

[1] Q.Y. Zhang, X.Y. Huang, Prog. Mater. Sci. 55 (2010) 353–427.
[2] Y. Peng, X. Chen, Z. Gao, Talanta 82 (2010) 1924–1928.
[3] T. Sreethawong, S. Chavadej, S. Ngamsinlapasathian, S. Yoshikawa, Solid State Sci. 10 (2008) 20–25.
[4] R. Bazzi, M.A. Flores-Gonzalez, C. Louis, K. Lebbou, C. Dujardin, A. Brenier, W. Zhang, O. Tillement, E. Bernstein, P. Perriat, J. Lumin. 102 (2003) 445–450.
[5] C. Soliman, Nucl. Instrum. Methods Phys. Res. B 251 (2006) 441–444.
[6] M. Zawadzki, L. Kepinski, J. Alloys Compd. 380 (2004) 255–259.
[7] B. Zhaorigetu, R. Ga, M. Li, J. Alloys Compd. 427 (2007) 235–237.
[8] A. Kosola, J. Päiväsaari, M. Putkonen, L. Niinistö, Thin Solid Films 479 (2005) 152–159.
[9] L. Kepinski, M. Zawadzki, W. Mista, Solid State Sci. 6 (2004) 1327–1336.
[10] M. Zawadzki, J. Alloys Compd. 451 (2008) 297–300.
[11] S.V. Chavan, P.U.M. Sastry, A.K. Tyagi, J. Alloys Compd. 456 (2008) 51–56.
[12] B.M. Nagabhushana, Ph.D. Thesis, Bangalore University, 2008.

[13] A. Jagannatha Reddy, M.K. Kokila, H. Nagabhushana, J.L. Rao, B.M. Nagabhushana, C. Shivakumara, R.P.S. Chakradhar, Spectrochim. Acta A 79 (2011) 476–480.
[14] G.K. Willamson, W.H. Hall, Acta Metall. 1 (1953) 22–31.
[15] J. Rodriguez-Carvajal, Full Proof 2000: A Program for Rietveld, profile matching and Integrated Intensity Refinements for X-ray and Neutron data, Version 1.6, Laboratoire Leon Brillounin, Gif sur Yvette, France, 2009.
[16] R.W.G. Wyckoff, Crystal Structures, vol. 2, Inter Science, New York, 1964, pp. 4–5.
[17] B. Umesh, B. Eraiah, H. Nagabhushana, B.M. Nagabhushana, G. Nagaraja, C. Shivakumara, R.P.S. Chakradhar, J. Alloys Compd. 509 (2011) 1146–1151.
[18] F. Rouquerol, J.R. Rouquerol, K. Sing, Adsorption by Powders and Porous Solids; Principles, Methodology and Applications, Academic press, San Diego, 1999.
[19] S. Phoka, P. Laokul, E. Swatsitang, V. Promarak, S. Seraphin, S. Maensiri, Mater. Chem. Phys. 115 (2009) 423–428.
[20] I. Kosacki, T. Suzuki, H.U. Anderson, P. Colomban, Solid State Ionics 149 (2002) 99–105.
[21] Z. Wang, Z. Quan, J. Lin, Inorg. Chem. 46 (13) (2007) 5237–5242.
[22] N. Dhananjaya, H. Nagabhushana, B.M. Nagabhushana, R.P.S. Chakradhar, C. Shivakumara, B. Rudraswamy, Physica B 405 (2010) 3795–3799.
[23] L.K. Pan, Q. Sun Chang, C.M. Li, J. Phys. Chem. B 108 (2004) 3404–3406.
[24] J. Tauc, in: F. Abeles (Ed.), Optical Properties of Solids, North-Holland, Amsterdam, 1970.
[25] N. Dhananjaya, H. Nagabhushana, B.M. Nagabhushana, B. Rudraswamy, C. Shivakumara, R.P.S. Chakradhar, J. Alloys Compd. 509 (2011) 2368–2374.
[26] S.K. Sharma, G.J. Exarhos, Solid State Phenom. 55 (1997) 32–37.
[27] Y. Repelin, C. Proust, E. Husson, J.M. Benny, J. Solid State Chem. 118 (1995) 163–169.
[28] A.S. Ahmed, M.M. Shafeeq, M.L. Singla, S. Tabassum, A.H. Naqvi, A. Azam, J. Lumin. 131 (2011) 1–6.
[29] A. Abragam, B. Bleaney, Electron Paramagnetic Resonance of Transition Ions, Clarendon Press, Oxford, 1970, p. 175.
[30] J.A. Weil, J.R. Bolton, J.E. Wertz, Electron Paramagnetic Resonance. Elementary Theory and Practical Applications, John Wiley, New York, 1994, p. 498.
[31] N.W. Aschcroft, N.D. Mermin, Solid State Physics, Harcourt College Publishers, 2001, p. 656.
[32] N. Dilawar, S. Mehrotra, D. Varandani, B.V. Kumaraswamy, S.K. Ha Idar, A.K. Bandyopadhyay, Mater. Charact. 59 (2008) 462–467.
[33] Y. Xu, J. Wu, W. Sun, D. Tao, L. Yang, Z. Song, S. Weng, Z. Xu, R.D. Soloway, D. Xu, G. Xu, Chem. Eur. J. 23 (2002) 5323–5331.